1-1-2014

Insight into instabilities in burning droplets

Ankur Miglani

Saptarshi Basu

Ranganathan Kumar
University of Central Florida

Insight into instabilities in burning droplets

Ankur Miglani, Saptarshi Basu, and Ranganathan Kumar

Citation: Physics of Fluids **26**, 032101 (2014); doi: 10.1063/1.4866866
View online: https://doi.org/10.1063/1.4866866
View Table of Contents: http://aip.scitation.org/toc/phf/26/3
Published by the American Institute of Physics

PHYSICS OF FLUIDS **26**, 032101 (2014)

Insight into instabilities in burning droplets

Ankur Miglani,[1] Saptarshi Basu,[1,a)] and Ranganathan Kumar[2]
[1]*Department of Mechanical Engineering, Indian Institute of Science, Bangalore 560 012, India*
[2]*Department of Mechanical and Aerospace Engineering, University of Central Florida, Orlando, Florida 32816, USA*

(Received 14 August 2013; accepted 7 February 2014; published online 3 March 2014)

The complex multiscale physics of nano-particle laden functional droplets in a reacting environment is of fundamental and applied significance for a wide variety of applications ranging from thermal sprays to pharmaceutics to modern day combustors using new brands of bio-fuels. Formation of homogenous nucleated bubbles at the superheat limit inside vaporizing droplets (with or without nanoparticles) represents an unstable system. Here we show that self-induced boiling in burning functional pendant droplets can produce severe volumetric shape oscillations. Internal pressure build-up due to ebullition activity ejects bubbles from the droplet domain causing undulations on the droplet surface and oscillations in bulk. Through experiments, we establish that the degree of droplet deformation depends on the frequency and intensity of these bubble expulsion events. In a distinct regime of single isolated bubble residing in the droplet, however, pre-ejection transient time is identified by Darrieus-Landau evaporative instability, where *bubble-droplet system* behaves as a *synchronized driver-driven system* with bulk bubble-shape oscillations being imposed on the droplet. The agglomeration of nanophase additives modulates the flow structures within the droplet and also influences the bubble inception and growth leading to different levels of instabilities. [http://dx.doi.org/10.1063/1.4866866]

I. INTRODUCTION

Thermo-physical processes and surface dynamics like shape oscillation mechanisms in vaporizing functional droplets at different spatio-temporal scales are pivotal to a diverse range of practical applications such as pharmaceutical drug delivery, innovative fuel injection strategies in combustors/premixers, spray combustion, surface patterning in micro channels, solution precursor plasma spray technique (SPPS) for thermal barrier coating, and biological crystal growth.[1–4] Controlling droplet deformations through physics based understanding at different scales can revolutionize many application areas. Single droplet represents the sub-grid unit of the spray. In practical spray systems, the dispersed droplets often experience severe shape deformation either through impingement impact on solid surfaces[5–15] or by excessive aerodynamic loading,[16–18] which may lead to their break-up. Break-up provides a natural mode of enhancing the surface area that facilitates an effective interfacial interaction. However, during the combustion of miscible, multicomponent liquid fuels, or emulsions, following primary atomization at the injector, the burning droplets may either undergo frequent local fragmentations to form μm-sized satellite droplets or break-up catastrophically during a single micro-explosion event.[19–21] These fragmentations are characterized by severe volumetric oscillations in droplets which coupled with the formation of μm-sized daughter droplets render an enhanced surface area for rapid vaporization and aid in homogenizing the fuel charge, i.e., effective mixing, thereby promoting clean and efficient combustion. These oscillation mechanisms thus

a)Author to whom correspondence should be addressed. Electronic mail: sbasu@mecheng.iisc.ernet.in

provide innovative means for manipulations at the droplet level, which is the fundamental building block of any liquid based combustion strategy.

The mechanism of preferential entrapment of high volatile species initiates homogeneous boiling within the droplet resulting in internal pressure upsurge.[22] This self-induced unstable situation may either cause sudden fissioning of the droplet following an intense micro-explosion or force the droplet into long-term, intense bulk-oscillations. Such bimodal droplet disruption behavior, also termed as secondary atomization, is characterized by continuous, multiple ejections of homogeneously nucleated micro-bubbles within the droplet, coupled with its own bulk deformation as burning advances. The intensity and frequency of bubble ejections is a strong function of the miscibility, volatility differentials and relative concentrations of component species, and diffusional resistance of the liquid phase (i.e., the liquid phase Lewis number Le_l).[23] The dependence of the severity of droplet disruption/microexplosion on the limit of superheat (thermodynamic metastable state) and its sensitivity to pressure have been previously reported for both miscible binary mixtures and water-in-n-alkane emulsions.[24–26] Based on the consideration of interfacial free energies, these studies revealed that boiling initiates principally at the water-hydrocarbon interface. Boiling in such cases may either be through the release of streams of tiny micro-bubbles or by growth of a single bubble at the interface. These investigations provide a comprehensive treatment on homogenous nucleation of bubbles and the corresponding upper temperature limits at which such micro-explosive effects trigger.[27] However, there is no data or analysis available in the current literature that provides insight into the bubble-droplet interactions and self-excited instabilities for burning droplets.

In addition to the aforementioned factors, particle aggregation either through perikinetic collisions, orthokinetic aggregation, or differential setting can significantly alter the homogenous ebullition process in burning nanofluid fuels droplets. In this scenario, the micro scale particle agglomerates may act as potential nucleation sites aiding heterogeneous nucleation. Any insight into the coupled phenomena of diffusional entrapment, ebullition activity, and shape oscillations in a burning droplet can have a far-reaching impact in various fields. Particularly newer blends of fuels can be engineered to undergo preferential instabilities leading to homogeneous combustion and higher efficiency.

In practice, droplet oscillation characteristics are significantly influenced by property variation and relative concentrations of the constituent species. For example, our recent study[28] on vaporizing, cerium nitrate precursor droplets showed that chemical transformation results in *in situ* production of nanoceria and gaseous NO_x. Subsequent pressure build-up leads the droplet into a non-periodic, swell-shrink cycle. In the case of non-reacting additives in a droplet (nanosilica,[29] for example), preferential transport and agglomeration of particles can induce rotation and reorientation, with the final precipitate morphing into a bowl or ring shaped structures. The instability mechanisms for a burning droplet, which remains largely unexplored, are very different from those of a non-burning droplet due to the bubble dynamics. The study of instabilities in a burning droplet, internal two-phase circulation, and the multiscale mechanisms responsible for shape oscillations form the basis for engineering newer fuels and better physics based system designs.

Specifically, we study three potential modes of bubble-droplet interaction during internal homogeneous boiling in a bi-component burning droplet and the ensuing shape deformation. We will show that in the first mode, bubble ejections induce surface corrugations on the droplet. The second intermittent mode is characterized by rapid collapse of the major bubble volume (termed as major ejection) that initiates large-amplitude surface undulations. The evaporative *Darrieus–Landau instability* (DL) at the bubble-droplet interface can also lead to volumetric droplet-shape oscillations, which constitutes the third mode. This is the first observation of such an instability and measurement of surface distortion in burning functional droplets, and its maximum growth rate and wave number are compared with the Landau theory. Additionally, it is demonstrated that the droplet internal circulation can be significantly altered by bubble ejections, facilitating intense mixing and redistribution of chemical species. This impacts droplet gasification, ebullition characteristics, and droplet deformation rate.

In this work, oscillatory characteristics of burning pendant droplets are investigated for two test fuels: (1) Nanoceria suspension (10 nm; 0.115 vol.% or 1 wt.%) in ethanol-water blend and (2) a pure ethanol-water blend.

II. EXPERIMENTAL METHODOLOGY

A. Fuel preparation

Two different functional droplets with constant composition of the bi-component base fuel (ethanol + water) were used in our experiments. Droplet 1 was a nanoceria suspension containing nanostructured ceria (CeO_2) as dispersed phase (average particle size of 10 nm-manufacturer specification), research grade ethanol (99.5% pure), and double distilled water as continuous phase at concentrations of 0.115 (1 wt.%,ceria), 84.12 (water), and 15.77 (ethanol) vol.%, respectively. The colloidal solution is prepared by diluting an aqueous suspension of initially 5 wt.% ceria (produced by chemical synthesis by Reinste Nano ventures) with research grade ethanol up to a final concentration of 1 wt.%. Subsequently, the mixture is subjected to ultrasound induced cavitation using an ultrasonic disruptor (Trans o sonic D120/P model) to homogenously disperse the particles and obtain a stable nanosuspension without adding any chemical surfactants. This is done at a sonicator frequency of 30 ± 3 kHz for about 30 min that consists of alternate cycles with 15 s of active pulsing 15 s apart. The resultant nanofluid exhibited no apparent precipitate formation due to particle aggregation or differential settling for ∼24 h, thus indicating a stable, long-term suspension with low sedimentation potential. Droplet 2 was a pure ethanol-water blend with volume concentrations of 84.23% and 15.77%, respectively.

B. Experimental apparatus and procedure

Experimental arrangement of a symmetrical, 50 μm tungsten crosswire configuration and a synchronized spark ignition-high speed imaging system for studying droplet shape deformation dynamics is shown schematically in Figure 1. A single channel, volume-calibrated micropipette (Variable volume "Biohit Proline Pipettor," 0.5–10 μl) was used to dispense the functional droplets at the crosswire junction (45°) that is symmetrically placed between spark ignition electrodes at 5 mm from each electrode tip. Although tungsten has high thermal conductivity, conduction effects in fibers with diameters below 100 μm are generally neglected.[23] Ignition of pendant fuel droplets was achieved in air at atmospheric pressure using high energy 6 kV spark transient of 50 ms.

A monochrome, ultra high-speed Photron SA5 camera fitted with a 1X Navitar microscopic lens (focal length – 50 mm) was used to record the droplet shape undulations at 15 000 fps (temporal resolution ∼66 μs) at image resolution of 1 024 × 1 024 pixels. Further, for precisely capturing the temporal evolution of key events like bubble incipience, coalescence/merging, and ejection, the droplet was illuminated volumetrically using a 250 W dual halogen white light source with 5 mm diameter coupled fiber optics. For visualizing internal circulation patterns the images were acquired at 1000 fps so that the bubbles exhibited streaklines. However, the velocity scales for internal liquid-phase convection were measured by tracking bubble motion (along vertical axis of symmetry) through short exposure images (15 000 fps: maximum exposure ∼66 μs; spatial resolution – 3.9 μm/pixel).

Finally, the recorded grey scale images of the droplet were contrast enhanced and converted to binary images using Otsu's thresholding technique.[30] The droplet shape was then reconstructed using an edge-detection routine inbuilt in the image analysis toolbox of MATLAB 7.10 to obtain its cross-sectional area. This dynamic time series data were used to obtain the corresponding data for instantaneous droplet diameter D (defined as the diameter of a projected area-equivalent-sphere) and spatial fluctuations in the centroid co-ordinates (this predicts the droplet oscillations in volume) during the burning process. The initial droplet volume and projection sphericity were 2.6 ± 0.02 μl (diameter: 1.7 ± 0.3 mm) and 0.96 ± 0.02, respectively. The relative error in the determination of squared non-dimensional diameter $(D/D_0)^2$ was calculated to be within ±3%. By contrast, the cross-sectional area of bubbles was measured for in-plane, tightly focused images at a temporal resolution of ∼10 ms using Photron Fastcam Viewer Ver.330 software with an uncertainty of ±0.05 mm in projected area diameters. Similar image processing (edge detection) was done for each bubble using MATLAB 7.10. The reported data on bubble statistics are ensemble over 5 experimental runs for each test droplet. Furthermore, first order estimate of bubble size magnification (m) due to lens effects (calculated using the convex, spherical refracting surface formula at room temperature

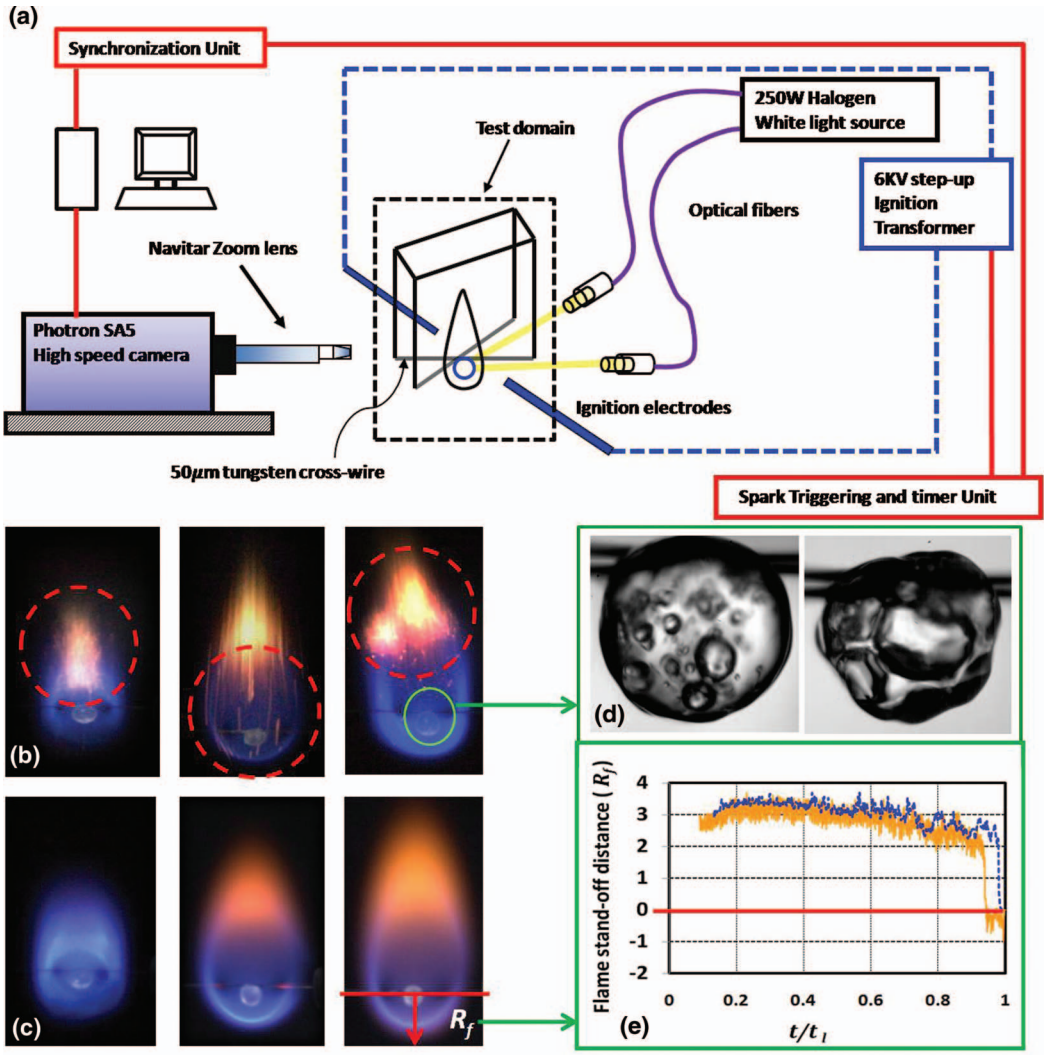

FIG. 1. Test facility. (a) Schematic of experimental set-up. Solid lines indicate synchronized spark control and image acquisition system. Dotted lines indicate high energy ignition system. (b) Instantaneous images of nanofuel droplet flame. Dotted circles indicate streaking of micro-scale particle aggregates. These are transported to the flame envelope by fragmented daughter droplets formed during localized, secondary break-up of the parent droplet, following bubble ejections. (c) Time frozen images of bi-component (ethanol-water) droplet flame without nanoadditives. (d) Instantaneous images of deformed droplet: acquired at 15 000 fps at spatial resolution of 3.9 μm/pixel. (e) Temporal variation of flame stand-off distance (R_f).

and neglecting the effect of surface undulations) indicated that m is ∼1.3, while the maximum variation in measured bubble diameter is within ±2.5% during the droplet lifecycle. Thus, uncertainty due to variation in refractive index (due to temperature/composition variation) has negligible effect on the relative trends of droplet void fraction while the bubble population remains unaltered.

III. RESULTS

Sections III A–III D describe the droplet lifecycle in detail. Ethanol-water blend with and without nanoceria additive was tested. Both types of test droplets undergo burning in the natural convection mode with a characteristic teardrop shaped, quasi-steady diffusion flame envelope showing maximum fluctuation of ±6% in the flame stand-off distance R_f (shown in Figure 1). Nanofuel droplet flame is additionally characterized by glowing particle agglomerates at flame envelope that escape continuously from the droplet domain along with satellite droplets formed during bubble ejections.

Besides, the droplets show diameter regression, volumetric oscillations, and bubble-induced instabilities with vigorous internal recirculation. Nanoparticle-laden droplets further show agglomeration with reduced regression rate and distinct bubble dynamics.

A. Ebullition process induced volumetric shape oscillations

Preferential entrapment initiated unstable boiling in burning functional droplets is expected to induce surface undulations of varying length scales due to continuous jetting out of the internally nucleated bubbles. This provides an intrinsic mechanism of triggering secondary break-up for maximizing the evaporative surface area. However, the growth of this self-induced instability is likely to be strongly influenced by the mode of nucleation and temporal evolution of internal bubble dynamics. We observed that the concurrent, multiple ejections of micro-bubbles triggered shortly after their incipience ($\sim$0.005 t_T) causing localized fragmentation of the primary droplet at several locations across the droplet surface. This localized break-up mode produced an *atomizing* or *sputtering effect* at the gas-liquid interface forming a sparse cloud of pinched-off daughter droplets around the parent droplet (shown in Video 1 of the supplementary material[31]). These bubble expulsion events occur continuously throughout the droplet lifecycle at millisecond timescale [O (2 ms)] with discharge velocities on the order of 5 m/s, however, with a varying intensity, that determines the degree of volumetric droplet-shape deformation. It depends on two key factors: (1) the internal pressure upsurge due to accumulated excess superheat and (2) the relative ratio of evacuated vapor space and the instantaneous droplet volume during ejection. This is quantified by an *ejection impact parameter*,

$$\alpha_{global}(t) = \left(\sum_{j=1}^{n} \frac{\pi}{6} d_{j,eject}^3\right)/\left(\frac{\pi}{6} D_{eject}^3\right), \qquad 0 \le \alpha_{global}(t) < 1,$$

where numerator represents the total vapor phase volume that collapses in the droplet interior during n simultaneous expulsion events at a given instant and d_j, D denote projected area diameters of jth bubble, parent droplet, respectively, at the pre-ejection instant. In essence, α represents a *deformation index* that measures the degree of distortion in the global droplet geometry following a bubble expulsion. Similarly $\alpha_{local}(t)$ represents a relevant parameter for localized single expulsion event. It is expected that α_{global} and α_{local} vary directly with the bubble ejection frequency (n per unit time), statistical bubble size distribution and inversely with the droplet surface regression rate. In particular, higher α values are seen in bubble size distributions with higher most probable bubble diameters. High magnitudes of $\alpha \to 1$ indicate major ejection events that are characterized by rapid discharge [O (1 ms)] of a considerable bubble volume ($\sim$0.5–0.6 times the instantaneous droplet volume) from the droplet interior. This causes volumetric shape deformation and leads to violent oscillations as the droplet suffers recoil/reactionary thrust following the ejection. Simultaneously, large-amplitude, low-wave number surface disturbances triggered by the rapid bubble collapse tend to induce large scale distortion of the surface segments, which are comparable in terms of length scale to the instantaneous droplet diameter. In this event, the droplet operational circularity may momentarily ($\sim$2 ms) decay to $\sim$0.7. This manifests as multiple time *axis-switching* and re-orientation of the droplet geometry within short time duration of about 10 ms as shown in Figure 2, while the droplet centroid traces a random trajectory with velocity and acceleration of the order of 5 m/s and 10^2 g, respectively (shown in Figure 3). On the other hand, $\alpha \ll 1$ signifies minor ejection events (low/intermediate intensity) which initiate small-scale surface roughening of the droplet and mild oscillations in volume. Figure 4 demonstrates the interaction of bubble and gas-droplet interface during one of the bubble expulsion events with $\alpha_{local} = 0.057$, that are fundamentally responsible for droplet surface wrinkling and analogous to the mechanism of bursting gas bubble at liquid free surface, as reported by Newitt *et al.*[32] Based on the relative strength of bubble ejections, i.e., α, the droplet deformation cycle can be divided into four regimes (Figure 5): (**I**) bubble nucleation, (**II**) onset of low intensity minor ejections ($\alpha_{local,\,max} \ll 0.1$); sluggish bubble growth, (**III**) intermediate intensity ejections ($0.1 < \alpha_{local,\,max} < 0.3$); regime with sharp decay in bubble population, and (**IV**)

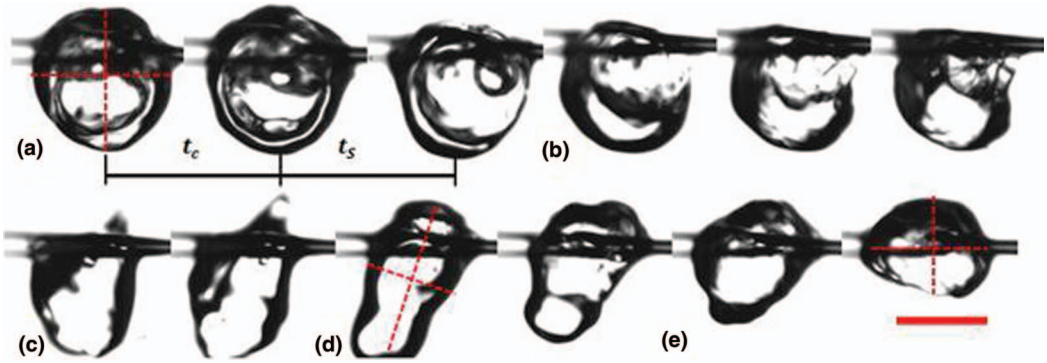

FIG. 2. Volumetric shape deformation during major bubble ejection. (a) Post coalescence bubble growth and droplet swelling, (b) collapse of vapor bubble space and volumetric droplet shrinkage, (c) formation of standing liquid jet and droplet shape transition to lenticular geometry, (d) post-ejection first axis-switching, and (e) post-ejection second axis-switching. For the image sequence the snapshots are at time instants (a) 0, 62.4, and 87.5 ms; (b) 97.8, 98, and 98.13 ms; (c) 98.8 and 99.25 ms; (d) 100 and 101.2 ms; and (e) 101.6 and 102 ms. The symbols t_c and t_s denote the time periods of constant and stagnated bubble growth, respectively. The scale bar equals 1 mm.

high intensity major ejections ($\alpha_{local,\,max} > 0.3$); rapid bubble growth with dominance of coalescence events.

High-speed images of a major ($\alpha_{local} = \alpha_{global} = 0.5$, Figure 2) and a minor ($\alpha_{local} = 0.057$, Figure 4) bubble ejection event illustrate an interesting comparison of the pre-ejection bubble coalescence-growth, subsequent collapse time-scales, and the resulting droplet shape deformation. It is observed that, while the pre-ejection bubble residence time (time elapsed since the initiation of last successful merging event prior to ejection) is two orders of magnitude lower for the minor bubble, the collapse time-scale and average collapse velocities are of the same order, i.e., O(1 ms) and O(5 m/s), respectively, for both types of ejections. These time and velocity scales were measured for 50 distinct ejection events with α_{local} ranging from 0.052 to 0.6 (maximum α_{local} observed in our experiments). This signifies that the proposed ejection impact parameter is rather independent of the vapor phase volume evacuation rate (i.e., average collapse velocity of bubble surface) but depends on the magnitude of this pre-ejection volume. In addition, occurrence of $\alpha \to 1$ events indicating the susceptibility to severe bulk deformation is favored in droplets with high

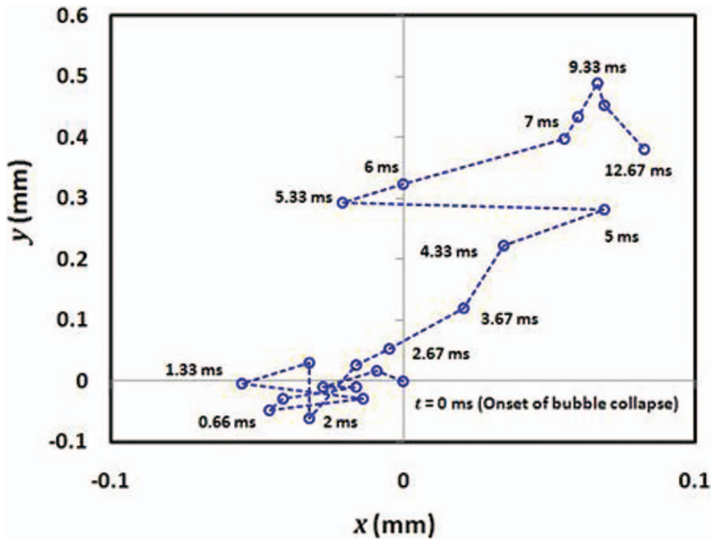

FIG. 3. Random trajectory traced by the droplet centroid following the onset of high intensity major bubble ejection in the single bubble regime ($\alpha_{\text{local}} = \alpha_{\text{global}} = 0.5$), indicating severe bulk oscillations of the droplet.

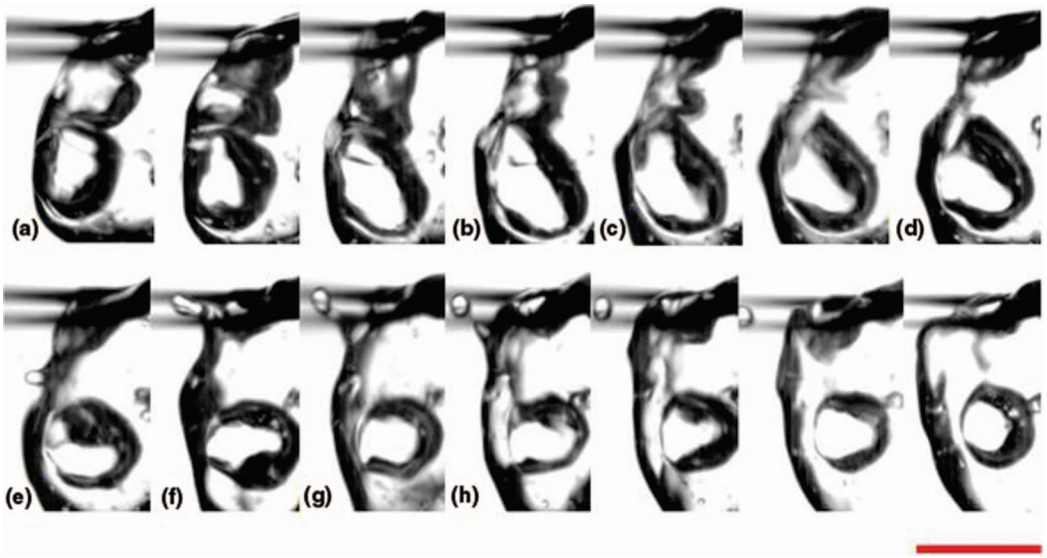

FIG. 4. Dynamic surface deformation during a minor bubble ejection. (a) Bubble coalescence, (b) lamella dome formation, (c) liquid sheet rupture and gas escape from within the bubble, (d) formation of surface crater, (e) depression fill-up and inception of standing liquid jet (ligament), (f) ligament growth and upward transport due to surface disturbance from adjacent minor ejection event, (g) onset of ligament break-up, and (h) ligament necking and daughter droplet pinch-off. For the image sequence snapshots are at time instants (a) 0, 0.2, and 0.47 ms, (b) 0.53 ms, (c) 0.6 and 0.67 ms, (d) 0.73 ms, (e) 0.87 ms, (f) 1.33 ms, (g) 1.47 ms, and (h) 1.6, 1.67, 1.8, and 2 ms. The local ejection impact parameter for this event is 0.057. The scale bar equals 1 mm.

surface regression rates and faster bubble growth rates. Moreover, as α_{global} and α_{local} magnitudes are expected to increase with time (since the droplet surface regresses and the mean bubble diameters grow continuously with time), volumetric oscillations also grow as the droplet proceeds towards extinction. These characteristics are apparent in Videos 2 and 3 of the supplementary material[31] and clearly illustrated in Figure 5 which shows the expected reverse trends of non-dimensional droplet

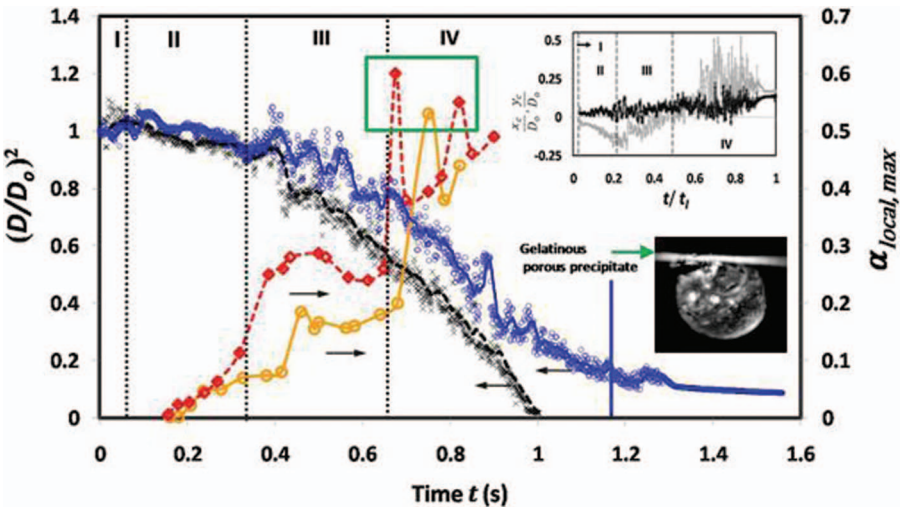

FIG. 5. Temporal variation of droplet diameter and maximum, local ejection impact parameter. Solid lines with open circle markers: for nanoceria dispersion droplet; flattening of droplet size for nanofuel droplet (blue curve) beyond ~1.2 s indicates reduced gasification rate and formation of gelatinous porous precipitate. Dotted lines with open rhombus markers: for ethanol-water droplet. Symbols I, II, III, and IV, respectively, indicate regimes of bubble nucleation with very low intensity minor ejections ($\alpha_{\text{local,max}} \ll 0.1$), low intensity minor ejections ($\alpha_{\text{local,max}} < 0.1$), intermediate intensity minor ejections ($0.1 < \alpha_{\text{local,max}} < 0.3$) and high intensity major bubble ejections ($\alpha_{\text{local,max}} > 0.3$). Solid rectangle in regime IV: sporadic major ejection events with single bubble within the droplet. Inset figure: black and gray lines, respectively, indicate the droplet centroid fluctuations in horizontal (x_c/D_o) and vertical (y_c/D_o) directions from the initial (x_c, y_c) ≡ (0, 0) co-ordinates.

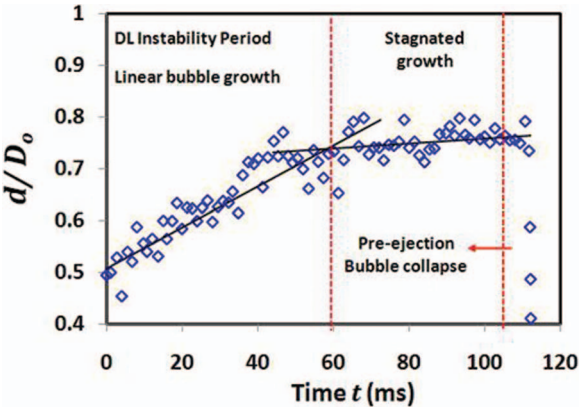

FIG. 6. Two-part dynamic growth behavior of major bubble in a single isolated bubble regime, prior to ejection.

diameter and $\alpha_{local,\,max}$ (maximum α value at given time instant) for both test droplets. It also shows a continuous increase in the amplitude of droplet centroid fluctuations (inset in Figure 5).

B. Transient evaporative instability (Darrieus-Landau instability)

In any random experimental run, a series of successful bubble merging may terminate into a single major bubble residing within the droplet. In this regime, the pre-major ejection time of ~90 ms is characterized by a two-part, distinct growth behavior of this single isolated bubble (shown in Figure 6). During initial phase (~60 ms) the evaporative front propagates into the liquid region at an average velocity of ~8.5 mm/s (i.e., bubble expansion velocity) as seen by a linear increase in the effective bubble diameter (d) that causes the droplet to swell by ~15%. In the second phase (~30 ms), however, the bubble growth decays rapidly and stagnates. In the initial phase, an evaporative instability is observed at the bubble-droplet interface. In the first phase, measured surface fluctuations at multiple angular locations across the bubble and primary droplet surface show an in-phase synchronized behavior with a dominant frequency of ~29 Hz. Figure 7(c) illustrates this coherent trend at a sample angular location ($\theta = 180^{\circ}$). This indicates that the large-scale wrinkling of the bubble surface due to the incipient instability wave is imposed or communicated directly to droplet surface as volumetric bubble-shape oscillations seem to be driving the bulk droplet-shape deformation. The bubble-droplet system thus behaves as a *self-excited coupled oscillator*. We propose that this self-induced transient instability is due to the Landau instability mechanism, described originally in reference to laminar flames[33] and subsequently modified by several investigators for unstable explosive boiling of droplets at the superheat limit.[34–37] In order to validate our hypothesis, the maximum wave number (k_{max}) and growth rate (ω_{max}) of interfacial evaporative instability are calculated based on the Landau-Darrieus theory:[33]

$$k_{\max} \cong \frac{2\rho_l v^2}{(3\varepsilon)\sigma}, \tag{1}$$

$$\omega_{\max} \cong \frac{2\rho_l v^3}{3\sigma(3\varepsilon)^{3/2}}, \tag{2}$$

where ρ_l, v, σ denote the liquid density, bubble growth velocity, and interfacial tension at the vapor-liquid interface (at 351.4 K, i.e., the boiling point of ethanol and a liquid phase volumetric concentration of 84.23/15.77 vol.% of ethanol/water), respectively, and $\varepsilon = \rho_v/\rho_l$ where ρ_v is the vapor bubble density. From experimental estimates of these parameters, the shortest instability initiation time is ~30 ms (i.e., $\omega_{max} \cong 34\ s^{-1}$) and the smallest spatial length-scale of surface distortion is ~0.8 mm. These values are consistent with the observed smallest resolvable corrugation length-scale of O (1 mm) and the disturbance wave frequency of ~29 Hz (obtained from the FFT

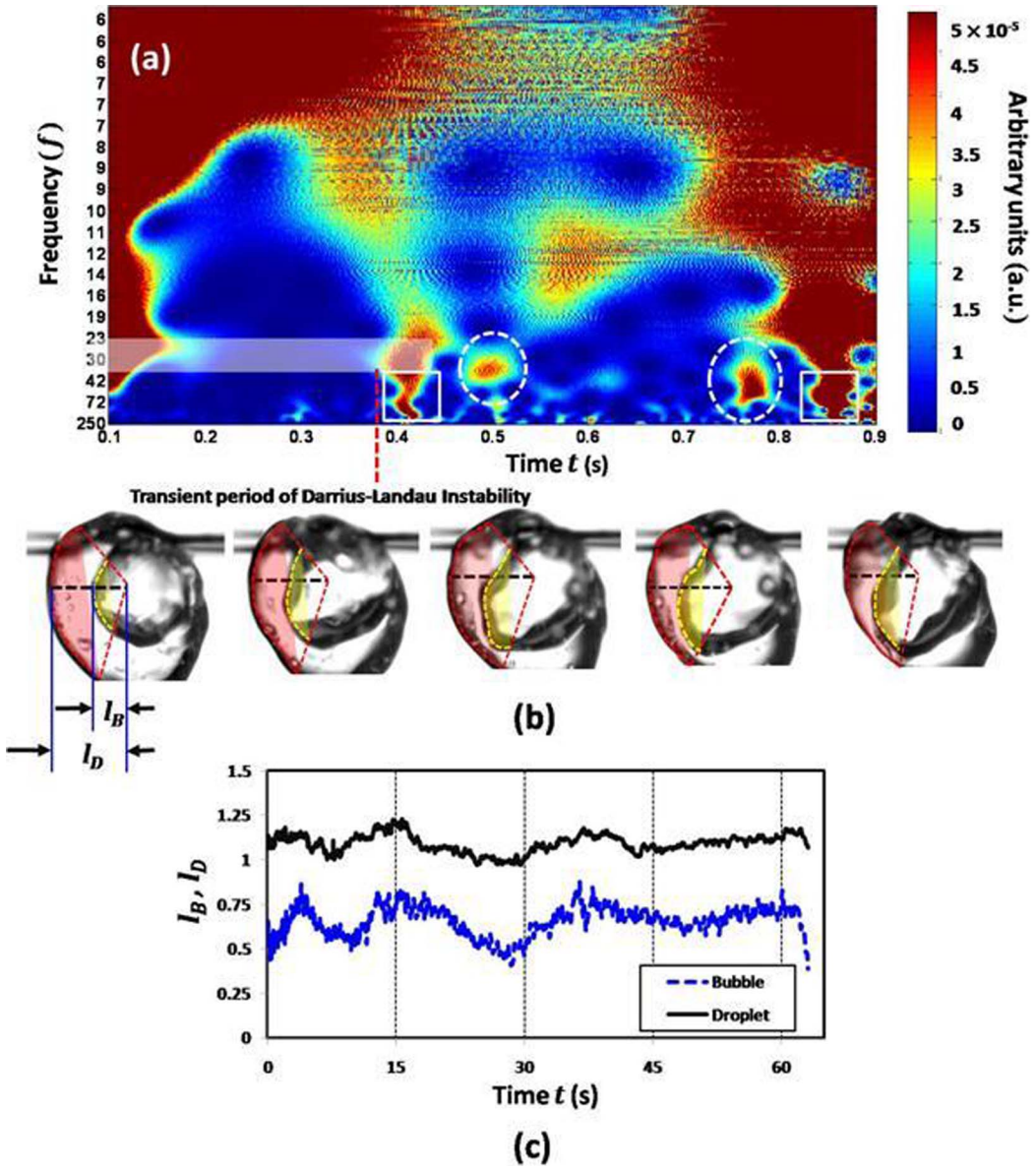

FIG. 7. (a) Continuous wavelet spectra of the droplet aspect ratio fluctuations. White band indicates 20–35 Hz pertinent frequency band corresponding to the maximum instability growth rate in DL instability regime. White squares denote the major ejection events in single bubble regime. Randomly scattered isolated patched of transient high frequencies correspond to low intensity minor ejections ($\alpha_{\text{local,max}} < 0.1$). White dotted circles correspond to intermediate intensity ejection events with $\alpha_{\text{local,max}}$ of 0.23 and 0.28. (b) Linear growth of single bubble inside droplet. Red and yellow segments, respectively, indicate the relative oscillations of droplet and bubble evaporative fronts. Symbols l_B and l_D denote the radial distance to the points on bubble and droplet surface, respectively, at a fixed angular location (shown here at 180°). (c) Temporal variation of l_B – dotted line, and l_D – solid line.

spectra of bubble surface segment oscillations at a fixed angular location). Furthermore, since the maximum instability growth rate and the wave number vary inversely with the interfacial tension, even with a 20% error in the estimate of interfacial tension, i.e., considering its variation temperature ranging from 300 K (pre-ignition or room temperature) to 351.4 K (boiling point of ethanol at atmospheric pressure) and composition, the magnitudes of k_{max} and ω_{max} are still within the DL instability limits ($\omega_{max} \sim 29$–$38\ \text{s}^{-1}$ and $k_{max} \sim 0.7$–0.9 mm).

Interestingly, the Continuous wavelet transform (CWT) spectra of droplet aspect ratio fluctuations (Figure 7(a)) show an increased dominance of ∼20–35 Hz pertinent frequency band in the pre-ejection transient time that is markedly close in agreement with the estimated instability growth rate. This validates our hypothesis that the baroclinic DL instability is indeed the key mechanism responsible for bulk droplet-shape oscillations in the initial, linear-growth phase of single bubble regime. This short period of active instability occurs intermittently during the droplet lifetime as shown in the wavelet spectra. Furthermore, the instability susceptibility index ($S = \tau.\omega_{max}$, where τ is the instability time period) that determines the amplification factor of the disturbances during the instability regime is estimated to be ∼1.8 in our experiments. Comparison of this index with that estimated by Sturtevant and Shepherd[36] for rapidly evaporating butanol, water, and liquid sodium droplets ($S = 2.9, 29, 2900$, respectively), indicates that burning functional droplets are only marginally unstable in the pre-major ejection transient phase. This is the first reported instance of DL instability in burning droplet under natural convection mode.

C. Regimes in ebullition activity and effects of nanophase additive

We have established that the *ejection impact parameter* is a key factor governing droplet deformation and oscillations in volume. However, in burning nanofuel droplet, particle-phase perikinetic aggregation kinetics may significantly modulate this parameter. This is due to the gradual formation a semi-solid porous crust of weakly bonded, micro-scale agglomerates that inhibits internal liquid fuel diffusion, thereby reducing the droplet gasification rate. This translate to a reduction in α as can be seen by a consistently lower value of $\alpha_{local,\ max}$ in case of nanofuel droplet (shown in Figure 5). Previous studies on combustion of nanoparticle laden droplets[38] have also shown that increase in surface concentration of nanophase due to vaporization and subsequent formation of porous shell impedes the transport of internally trapped liquid core towards the droplet surface resulting in a potential reduction in its burning rate. Besides, this gelatinous cocoon structure behaves like a low-stiffness elastic membrane that sustains the internal pressure build-up with bubbles trapped in the viscous core forcing the droplet into a non-periodic inflation/deflation cycle. This causes an expected reduction in the bubble ejection frequency with damped droplet-shape oscillations (shown in Video 4 of the supplementary material[31]).

Figure 8 shows distinct regimes in the ebullition activity based on the temporal evolution of bubble population (n) and droplet void fraction (ϕ) (shown in inset) in burning nanoceria-laden and conventional EW (Ethanol-Water) droplets. It is apparent that the bubble population is consistently higher in nanosuspensions for the entire droplet lifecycle and exhibits a skewed bell-shaped distribution. Following the initial transient period of bubble nucleation in regime I, the bubble population shows a sharp linear rise with nearly a ten-fold increase in the average bubble count. This corresponds to an average population growth rate of ∼1 bubble/ms in nanofuel droplet. By contrast, this magnitude is ∼4 times lower in traditional EW droplet. These values are ensemble-averaged over 5 experimental runs in droplets with initial volume and operational circularity of ∼2.6 μl and 0.96 ± 0.02, respectively. This drastic variation in the bubble population is observed under identical experimental conditions and indicates that the suspended nanophase additives possibly act as potential nucleation sites under volumetric heating by the surrounding flame envelope even at dilute concentrations (<1 vol.%). Thus, they induce a transition from homogeneous to heterogeneous nucleation mechanism which signifies a reduction in the degree of accumulated excess superheat and hence the internal pressure build-up within the droplet. This facilitates a decrease in the intensity of bubble ejection events. This is reflected by significant lower amplitude (∼20%–50%) of the transient spike in aspect ratio fluctuations (i.e., a major bubble ejection) of nanofuel droplet compared to EW droplet (shown in Figure 9).

Referring back to the discussion on bubble population, as the nucleated bubbles grow and bubble merging and ejection events become frequent, the bubble count attains maxima at ∼20% of the droplet lifetime before decaying rapidly. As expected, this regime (III) is characterized by synchronized, reversed trends of continuously increasing droplet void fraction and depleting bubble population. By contrast, regime II shows an increase in both parameters. For traditional EW droplets, these inverse trends continue to diverge for rest of the droplet lifecycle with final regime

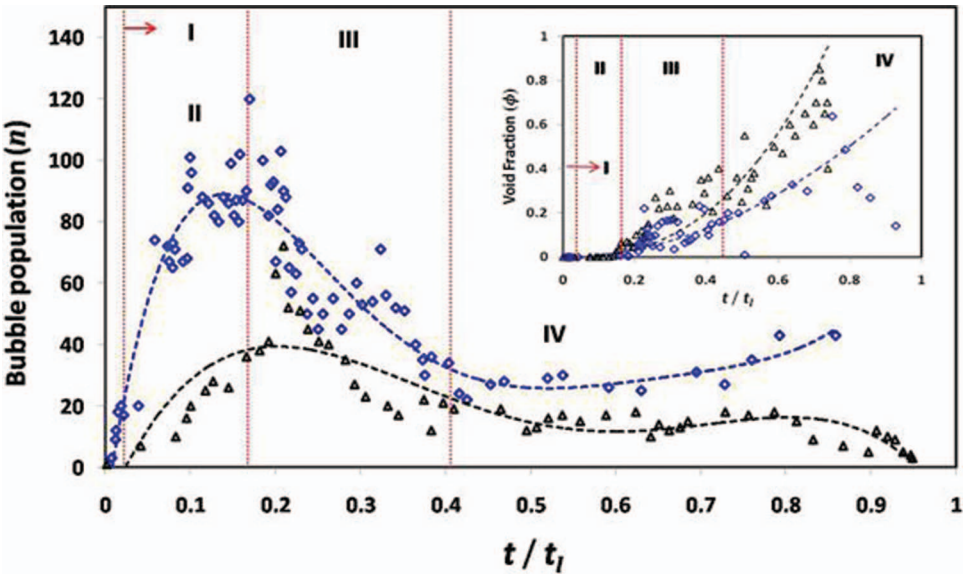

FIG. 8. Regimes in ebullition activity based on bubble population and droplet void fraction (shown in inset). Dotted lines with open rhombus markers: nanoceria dispersion droplet. Dotted lines with open triangle markers: for ethanol-water droplet (without nanoadditives). Symbols I, II, III, and IV denote the regimes that correspond to similar regimes in Figure 3 based on maximum, local ejection impact parameter. Time is normalized with the total droplet lifetime.

IV being characterized by multiple cascades of rapidly occurring bubble merging events. This leads to the frequent formation of large bubbles with projected diameters of ∼0.5–0.8 times the instantaneous droplet diameter (D), thereby aiding intense pressure build-up and subsequent high intensity ejections. This features low-wave number high-amplitude surface undulations [O (1 mm)] comparable in length scale to D and large scale spatial shifting of the centroid (∼0.5 D_o in <10 ms). However, in nanosuspension droplets, the bubble population nearly stagnates. This anomalous behavior is due to the increased tendency of bubble entrapment in the gel-type cocoon structure that is formed due to enrichment of surface concentration of particles (since liquid phase gets gradually depleted from the droplet domain). Droplet void fraction (ϕ) is defined as the fraction of

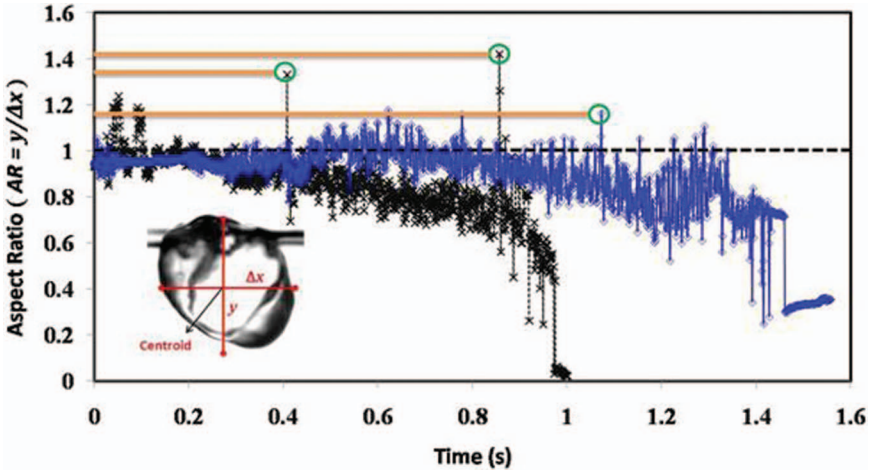

FIG. 9. Time history of droplet aspect ratio fluctuations. Solid line with open rhombus markers: nanoceria dispersion droplet, dotted line with cross markers (X): conventional ethanol-water blend. Inset shows the droplet aspect ratio. Circles indicate high intensity major bubble ejections of a single bubble residing within the droplet. Solid lines corresponding to these circles indicate relative degree of geometrical deformation suffered by the droplet during these ejections in both test droplets.

instantaneous droplet volume, V, occupied by the bubbles, and represents the combined contribution of the bubble crowd density (i.e., n/V) and the bubble size distribution towards instantaneous vapor space volume. ϕ shows a continuous growth with time. Note that higher ϕ is favored in functional droplets with faster growth rate of bubbles and their population and with rapid droplet-surface regression, i.e., factors that facilitate higher $\alpha \rightarrow 1$. Therefore, ϕ represents a kind of *secondary, deformation susceptibility index*; primary being α, where large $\phi \rightarrow 1$ is an indirect indicator of high pressure build-up within the droplet and hence signifies an unstable droplet state with heightened probability of undergoing severe shape deformation. Thus, the coupled effects of a consistent increase in ϕ and continuous regression of the droplet surface indicates that the probability of occurrence of high α events is enhanced as the droplet nears extinction (shown previously by continual rise in $\alpha_{local,\ max}$ magnitude with time in Figure 5). This lends additional support to our observations that the burning functional droplets exhibit increased susceptibility to self-excited bulk shape oscillations at later stages of their lifecycle. These regimes in boiling activity of nanofuels correspond closely to droplet deformation regimes shown in Figure 5. Besides, it is important to note that the presence of support fiber provides a surface that promotes heterogeneous nucleation thereby resulting in small-droplet ejections. However, the effect of the fiber on bubble dynamics is hard to quantify compared to a contact free environment (like drop tower or acoustic levitation). It is expected that since all droplets are subject to the same pendant condition, the physics and observations illustrated in this work will remain unaltered including the deformation regimes and DL instability.

D. Internal liquid-phase circulation

Typical regimes in the sequential transition of internal recirculation from incipience of a central toroidal vortex ring to its complete breakdown either to a disorderly two-phase bubbly flow or to a damped viscous flow (nanofuels) are shown in Figure 10. During the transient heat-up period and the initial phase of droplet gasification, i.e., $\frac{\Delta(D^3)}{D_0^3} < 0.05,\ \Delta t \sim 0.35\ t_l$, where D and D_o denote the instantaneous and initial droplet diameters, respectively, and the first occurrence of a single toroidal vortex is observed at time $t \sim 0.0035\ t_l$ following homogenous bubble nucleation. The velocity along the central axis (U_{lc}, maximum circulation velocity) of the droplet is of the order of 90 mm/s. At a later stage ($t \sim 0.25\ t_l$), this toroidal structure exhibits an intermittent oscillatory behavior with small amplitude angular and circumferential oscillations about the vertical axis of symmetry with U_{lc} escalating to ~150 mm/s. U_{lc} is estimated from the velocity of nucleated micro-bubbles that act as primary flow tracers in the present experiment and enable internal flow visualization. Under the assumption of axisymmetric free-convection around a vaporizing spherical droplet and using shear stress continuity at gas-liquid interface, maximum liquid-phase velocity at the droplet surface is given by[39]

$$U_{\max,s} = \frac{1}{6\pi}\frac{\mu_g}{\mu_l} C_f \mathrm{Re}\ U_{rel} = U_c, \tag{3}$$

where $C_f = 12.69\ \mathrm{Re}^{-2/3}/(1 + B_m)$[40] represents the friction drag coefficient and μ, B_m, Re, U_{rel}, and U_c denote the dynamic viscosity, mass transfer number, Reynolds number, relative gas/droplet velocity, and liquid phase circulation velocity. The subscripts g, l denote gas and liquid phase, respectively. For a pendant droplet of ~1.7 mm initial diameter and $U_{rel} = O(1$ m/s) (measured experimentally from high speed imaging of streaking nanoparticles or particle aggregates at the flame envelope), the maximum Reynolds number is estimated to be around 20–30 during the initial vaporization period ($\Delta t \sim 0.35\ t_l$). Based on this analysis U_c is calculated to be ~40–50 mm/s that matches with the experimentally determined internal circulation velocities of about 90–150 mm/s. Further, this initial regime is characterized by the onset of multiple, minor bubble ejections that result in small-scale droplet surface undulations that lead to deviations from the original projection sphericity (within ±2%). The droplet centroid also displaces horizontally by ~0.15 mm. At later time instants $t \sim 0.3\ t_l$, however, the increased intensity and rapidity of these expulsion events causes momentary rotation, reorientation, and deformation of the toroidal vortex that eventually collapses and transitions to solid body rotation about an inclined horizontal axis with rotational velocity of

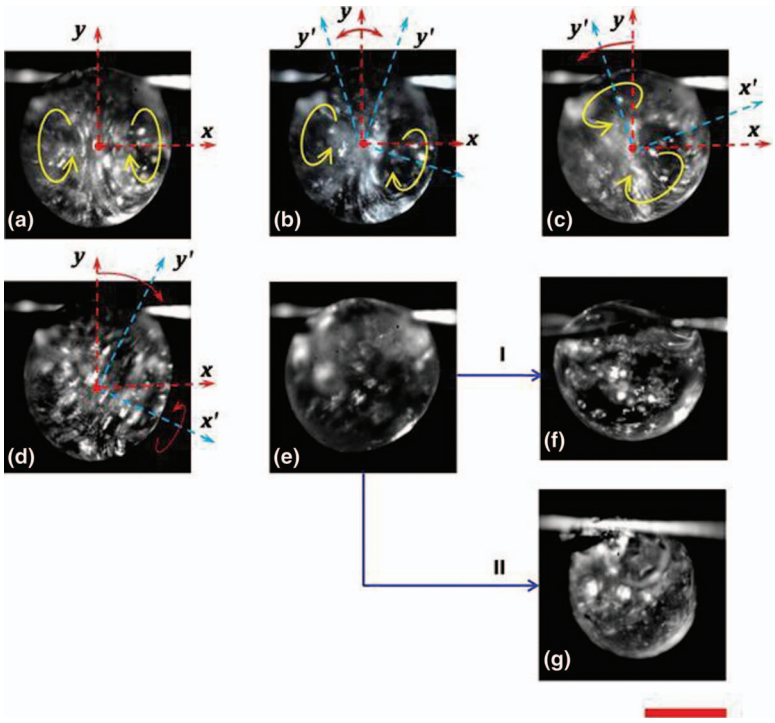

FIG. 10. Dynamic regime transition of internal circulation in a burning functional droplet under natural convection mode. (a) Inception of toroidal recirculation structure, (b) small amplitude angular and azimuthal oscillations about vertical axis of symmetry and temporary tilting of toroidal vortex, (c) rotational transition of the axis of circulation from initial vertical axis to an inclined horizontal axis, (d) collapse of the toroidal ring and transition to solid body rotation, (e) disintegration of the organized solid body rotation to disorderly flow pattern, (f) continual disorderly flow, and (g) damped viscous flow. Symbols I and II indicate distinct paths of internal motion in pre-extinction phase for conventional ethanol-water and nanoceria dispersion droplets, respectively. Symbols y and x denote the initial vertical and horizontal axes and y', x' indicate there instantaneous orientation. Internal arrows mark the instantaneous direction of liquid circulation. The scale bar equals 1 mm.

about ∼200 mm/s. This reorientation of the toroidal axis is characterized by a large-scale swerving of the toroidal vortex ring prior to transition to solid body rotation. Subsequently, as the nucleated bubbles coalesce and grow to larger effective diameters, the severity of bubble jetting increases since the effective length-scale of perturbed droplet surface varies directly with the pre-ejection volume occupied by the discharged bubble. However, at a certain critical threshold intensity and frequency of these minor ejections, the solid body rotation finally disintegrates into a complex, time-varying chaotic flow pattern which persists for the remainder of the droplet's lifetime.

Vigorous mixing in this bubbly flow regime may be attributed to a complex interplay of local and bulk liquid motion that produces a spatio-temporally varying churning effect. Localized liquid movement is triggered by the ejecting bubbles that essentially behave as miniature liquid agitators or micro-pumps moving fluid parcels equivalent to their own volume while the bulk convection occurs due to (a) disturbance waves initiated by perturbed droplet surface during bubble ejections and (b) cumulative effect of Marangoni convection, gas expansion, and viscous shear at the gas-liquid interface. In this regime the droplet oscillates violently in all x, y, and z directions and exhibits large-scale volumetric shape deformation as surface corrugations grow both in amplitude and wavelength.

In the nanofuel droplet, however, the particle phase aggregation kinetics leads to increased fluid viscosity in the droplet domain which gradually dampens and finally stagnates the internal motion with trapped bubbles in the gelatinous viscous structure (shown in Video 5 of the supplementary material[31]).

IV. CONCLUSION

The principal problem affecting several industries (for example, thermal spray, pharmaceutics, gas turbine combustors, aero-engines) is the lack of understanding of the thermo-physical processes at the droplet scale particularly for reacting systems. As a result, the tasks of creating new synthetic fuels or generating high quality coatings or custom controlled drugs become onerous with time consuming trial and error based experimentation. In this work, we have made an attempt to put forward mechanisms of bubble-droplet interactions that can potentially lead to better understanding of combustion phenomenon. The current research offers a first of its kind diagnostic insight into the physics of a burning droplet subjected to instabilities of various kinds at different length and time scales.

Diffusional entrapment driven internal boiling induces geometrical deformation in burning functional droplets through three pertinent modes of bubble-droplet interaction. First, low intensity ($\alpha \ll 1$) continual bubble ejections occurring at short timescale of O (2 ms) perturb the droplet surface segments locally around the bubble discharge locations, thereby triggering small-scale surface roughening. An intermittently occurring second mode is characterized by high intensity ($\alpha \rightarrow 1$) bubble ejections that initiate large-scale corrugation of the droplet surface and violent, non-periodic oscillations in bulk. Distinct regime of single major bubble ($d^3/D^3 \sim 0.4$–0.6) is identified to be evaporative *Darrieus–Landau instability* during the pre-ejection phase, which constitutes the third feasible mode. We calculated the maximum instability growth rate ($\sim$34 s^{-1}) and wave number ($\sim$0.8 mm) based on Landau theory that are consistent with our experimental estimates obtained from frequency spectra of coherent bubble-droplet surface segment oscillations (at multiple angular

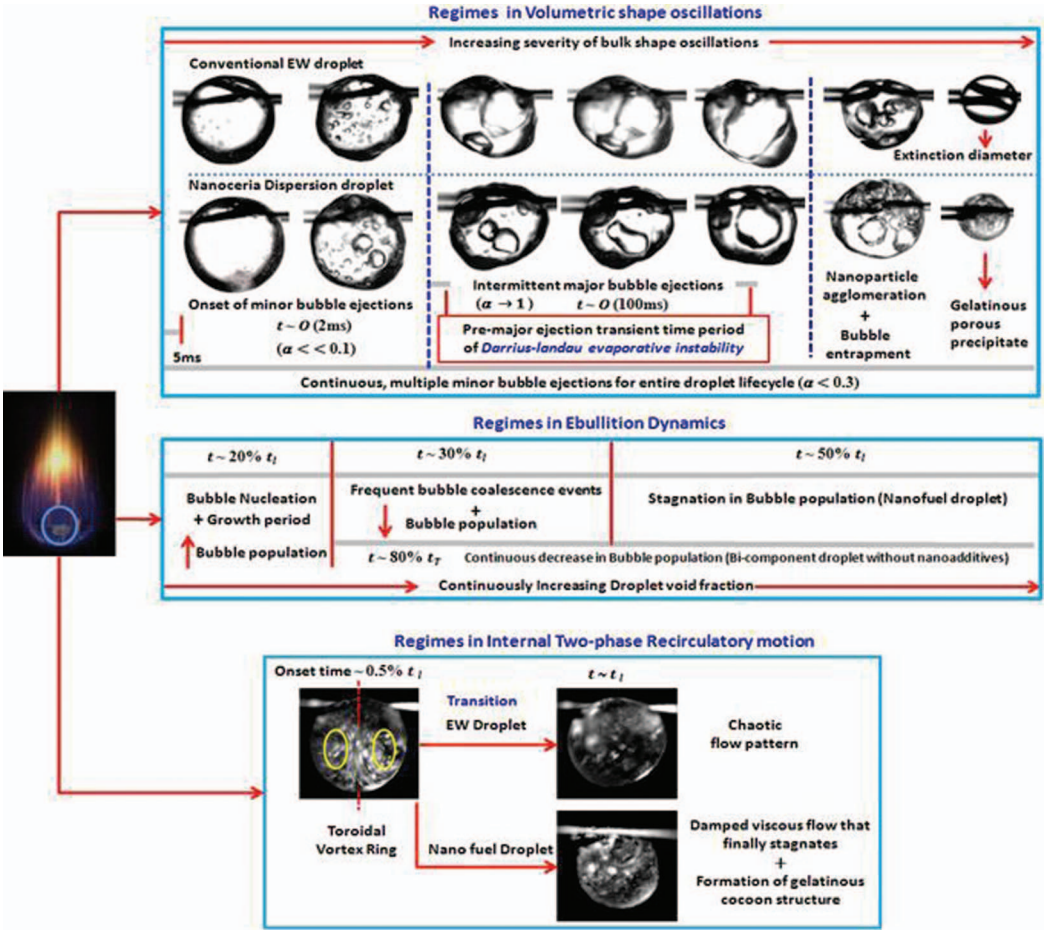

FIG. 11. Schematic showing the summary of results. Grey bars indicate the timescales of various events.

locations: Figure 7(c)). Indeed, in this transient instability time period, the CWT of droplet aspect ratio fluctuation (Figure 7(a)) exhibits dominant frequency within the same band ($\sim$20–35 s^{-1}).

As the droplet progresses towards extinction, the increased dominance of high intensity ejections severely deform the droplet. This observed transition from low to high intensity ejections, i.e., shifting dominance from $\alpha < 0.1$ to $\alpha \rightarrow 1$ events is coherent with the dynamic regime transformation of bubble statistics (shown in Figures 5 and 8). In particular, beyond $\sim$0.2 t_l, the decaying bubble population and consistently rising ϕ translate to higher average bubble diameters which favor occurrence of high α events.

Interestingly, in nanofuel droplets, the suspended nanoparticles behave as active nucleation sites, which is substantiated by a two-order, higher magnitude of average bubble population growth during initial nucleation-growth period as shown in Figure 8. This aids heterogeneous nucleation, which restricts the extent of stored superheat and coupled pressure build-up, thereby promoting lower intensity ejections in nanosuspensions compared to traditional EW droplet (demonstrated in Figure 5). This illustrates that it is possible to control the extent of atomization using nanoadditives in minute quantities even under burning conditions. Such complex interplay of multiscale physical phenomenon governing the volumetric shape oscillation dynamics in burning functional droplets is summarized in Figure 11.

[1] A. Ozturk and B. M. Cetegen, "Morphology of ceramic particulates formed in a premixed oxygen/acetylene flame from liquid precursor droplets," Acta Mater. **53**(8), 2531–2544 (2005).
[2] S. Basu and B. M. Cetegen, "Modeling of liquid ceramic precursor droplets in a high velocity oxy-fuel flame jet," Acta Mater. **56**, 2750–2759 (2008).
[3] K. V. Wong and O. De Leon, "Applications of nanofluids: Current and future," Adv. Mech. Eng. **2010**, 519659.
[4] M. Eslamian and M. Shekkariz, "Recent advances in nanoparticle preparation by spray and microemulsion methods," Recent Patents Nanotechnol. **3**(2), 99–115 (2009).
[5] A. Wright, "Fluid mechanics: Impact factors," Nature (London) **419**, 576 (2002).
[6] S. L. Manzello and J. C. Yang, "On the collision dynamics of water droplet containing an additive on a heated solid surface," Proc. R. Soc. London A **458**, 2417–2444 (2002).
[7] S. Mandre, M. Mani, and M. P. Brenner, "Precursors to splashing of liquid droplets on a solid surface," Phys. Rev. Lett. **102**, 134502 (2009).
[8] G. Juarez, T. Gastopoulos, Y. Zhang, M. L. Siegel, and P. E. Arratia, "Splash control of drop impacts with geometric targets," Phys. Rev. E **85**, 026319 (2012).
[9] M. M. Driscoll, S. C. Stevens, and S. R. Nagel, "Thin film formation during splashing of viscous liquids," Phys. Rev. E **82**, 036302 (2010).
[10] E. Villermaux and B. Bossa, "Droplet fragmentation on impact," J. Fluid Mech. **668**, 412–435 (2011).
[11] G. Lagubeau, M. A. Fontelos, C. Josserand, A. Maurel, V. Pagneux, and P. Petitjeans, "Spreading dynamics of drop impacts," J. Fluid Mech. **713**, 50–60 (2012).
[12] C. Josserand, L. Lemoyne, T. Troeger, and S. Zalseki, "Droplet impact on a dry surface: Triggering the splash with a small obstacle," J. Fluid Mech. **524**, 47–56 (2005).
[13] A. L. Yarin and D. A. Weiss, "Impact of drops on solid surfaces: Self similarity capillary waves, and splashing as a new type of kinematic discontinuity," J. Fluid Mech. **283**, 141–173 (1995).
[14] A. L. N. Moreira, A. S. Moita, and S. Chandra, "Droplet impact on solid surface," in *Handbook of Atomization and Sprays-theory and Applications*, edited by N. Ashgriz (Springer, New York, USA, 2011).
[15] S. Chandra and C. T. Avedisian, "On the collision of a droplet with a solid surface," Proc. R. Soc. London A **432**, 13–41 (1991).
[16] B. E. Gelfand, "Droplet breakup phenomenon in flows with velocity lag," Prog. Energy Combust. Sci. **22**(3), 201–265 (1996).
[17] L. P. Hsiang and G. M. Faeth, "Near-limit drop deformation and secondary break-up," Int. J. Multiphase Flow **18**(5), 635–652 (1992).
[18] D. R. Guildenbecher, C. Lopez-Rivera, and P. E. Sojka, "Droplet deformation and breakup," in*Handbook of Atomization and Sprays-theory and Applications*, edited by N. Ashgriz (Springer, New York, USA, 2011).
[19] C. H. Wang, H. Q. Liu, and C. K. Law, "Combustion and microexplosion of freely falling multicomponent droplets," Combust. Flame **56**, 175–197 (1984).
[20] C. H. Wang and C. K. Law, "Microexplosion of fuel droplets under high pressure," Combust. Flame **59**, 53–62 (1985).
[21] J. C. Lasheras, A. C. Fernando-Pello, and F. L. Dryer, "On the disruptive burning of free droplets of alcohol/n-paraffin solutions and emulsions," Proc. Combust. Inst. **18**, 293–305 (1981).
[22] C. K. Law, "Internal boiling and superheating in vaporizing multicomponent droplets," AIChE J. **24**(4), 626–632 (1978).
[23] C. K. Law, *Combustion Physics* (Cambridge University Press, New York, USA, 2006).
[24] C. T. Avedisian and I. Glassman, "High pressure homogeneous nucleation of bubbles within superheated binary liquid mixtures," J. Heat Transfer **103**(2), 272–280 (1981).
[25] C. T. Avedisian and I. Glassman, "Superheating and boiling of water in hydrocarbons at high pressures," Int. J. Heat Mass Transfer **24**(4), 695–706 (1981).

[26] C. T. Avedisian and R. P. Andres, "Bubble nucleation in liquid-liquid emulsions," J. Colloid Interface Sci. **64**(3), 438 (1978).
[27] C. T. Avedisian, "The homogeneous nucleation limits of liquids," J. Phys. Chem. Ref. Data **14**(3), 695–720 (1985).
[28] A. Saha, S. Basu, C. Suryanarayana, and R. Kumar, "Experimental analysis of thermo-physical processes in acoustically levitated heated droplets," Int. J. Heat and Mass Transfer **53**, 5663–5674 (2010).
[29] R. Kumar, E. Tijerino, A. Saha, and S. Basu, "Structural morphology of acoustically levitated and heated nanosilica droplet," Appl. Phys. Lett. **97**, 123106 (2010).
[30] N. Otsu, "Threshold selection method from gray-level histograms," IEEE Trans Syst. Man Cybern **9**(1), 62–66 (1979).
[31] See supplementary material at http://dx.doi.org/10.1063/1.4866866 for Video 1: Secondary atomization of the parent droplet producing sputtering effect at the gas-liquid interface due the formation of pinched-off daughter droplets. Video 2: small scale corrugation of the droplet surface in regime **II**. Video 3: Large amplitude, low-wave number corrugation of the droplet surface in regimes **III** and **IV**. Video 4: Formation of a gelatinous viscous crust due to particle agglomeration resulting in bubble entrapment, reduced bubble ejection frequency and damped droplet-shape oscillations. Video 5: Damping of the internal liquid motion till final stagnation in regime **IV** for a nanofuel droplet as fluid becomes more viscous (due to increased dominance of particle aggregation).
[32] D. M. Newitt, N. Dombrowski, and F. H. Knelman, "Liquid entrainment 1. The mechanism of drop formation from gas or vapor bubbles," Trans. Inst. Chem. Eng. **32**, 244 (1954).
[33] L. D. Landau and E. M. Lifshitz, *Fluid Mechanics* (Pergamon Press, London, UK, 1959).
[34] J. E. Shepherd, "Dynamics of vapor explosions: Rapid evaporation and instability of butane droplets exploding at the superheat limit," Ph.D. thesis, California Institute of Technology, 1981.
[35] D. Frost and B. Sturtevant, "Effects of ambient pressure on the instability of a liquid boiling explosively at the superheat limit," J. Heat Transfer **108**, 418 (1986).
[36] J. E. Shepherd and B. Sturtevant, "Rapid evaporation at superheat limit," J. Fluid Mech. **121**, 379 (1982).
[37] J. G. Xie, T. E. Ruekgauer, and R. L. Armstrong, "Evaporative instability in pulsed laser-heated droplets," Phys. Rev. Lett. **66**, 2988 (1991).
[38] Y. Gan and L. Qiao, "Combustion characteristics of fuel droplets with addition of nano and micron-sized aluminum particles," Combust. Flame **158**, 354–368 (2011).
[39] W. M. Sirignano, *Fluid Dynamics and Transport of Droplets and Sprays* (Cambridge University Press, New York, USA, 2010).
[40] M. Renksizbulut and M. C. Yuen, "Experimental study of droplet evaporation in high temperature air stream," J. Heat Transfer **105**, 384–388 (1983).